

Supplementary Information

Boosting Stability of Non-Precious Fuel Cell Catalyst via Triple Pyrolysis and Stacking-Pore Regulation

Xizhi Yang, Yanyan Xie, Zhenyang Xie, Jian Wang*, Wei Ding*

State Key Laboratory of Advanced Chemical Power Sources, College of Chemistry and Chemical Engineering; Center of Advanced Electrochemical Energy (CAEE), Institute of Advanced Interdisciplinary Studies, Chongqing University, Chongqing, China. Chongqing 400044, China.

E-mail: wangjian-fc@cqu.edu.cn; dingwei128@cqu.edu.cn

Experimental Section

Chemicals

2-Methylimidazole ($C_4H_6N_2$, 99.0%) and Ferrous acetate ($Fe(OAc)_2$) were purchased from Sigma-Aldrich. 2-Methylimidazole ($C_4H_6N_2$) and Phenanthroline ($C_{12}H_8N_2$) were purchased from Shanghai Aladdin Biochemical Technology Co., Ltd. Zinc nitrate hexahydrate ($Zn(NO_3)_2 \cdot 6H_2O$), Zinc acetate dihydrate ($Zn(OAc)_2 \cdot 2H_2O$), Potassium hydroxide (KOH), methanol (CH_3OH), ethanol (C_2H_6O), and isopropyl alcohol (C_3H_8O) were obtained from Chongqing Chuandong Chemical Co., Ltd, China. Commercial Pt/C (20 wt%), Commercial PtRu/C (75 wt%) catalyst was purchased from Johnson Matthey. Nafion-HP membrane and Nafion solution were purchased from DuPont. Piper Ion-A20- HCO_3 membrane and PAP-TP-100 were purchased from Versogen. All chemicals were of analytical grade and used without further purification.

Synthesis of Fe-N-C-70 Catalyst

A methanol solution (100 mL) containing $Zn(NO_3)_2 \cdot 6H_2O$ (2.94 g) was added to another methanol solution (100 mL) containing 2-methylimidazole (3.24 g) under continuous stirring. The mixture was stirred for 6 hours at room temperature. The resulting white precipitate was collected by centrifugation, washed three times with methanol, and dried under vacuum at $80^\circ C$ to obtain ZIF-8₇₀. The obtained ZIF-8₇₀ powder underwent preheating treatment in a tube furnace under nitrogen atmosphere at $650^\circ C$ for 1 hour (heating rate: $5^\circ C/min$). Subsequently, ZIF-8_{preheated} (100 mg) was dispersed in deionized water (20 mL) and sonicated for 30 minutes, followed by the addition of ferrous acetate (15 mg) and 1,10-phenanthroline (56 mg). The mixture was stirred for 24 hours. The product was collected by centrifugation, dried, and pyrolyzed under nitrogen atmosphere at $1000^\circ C$ for 60 minutes (heating rate: $5^\circ C/min$). When the heating was completed and the temperature dropped to $800^\circ C$, ammonia was introduced into the tube, and the furnace was kept at this temperature for 30 minutes. After cooling to room temperature, the product was ground to obtain the final Fe-N-C-70 catalyst with an average particle size of 70 nm.

Synthesis of Fe-N-C-150 Catalyst

A methanol solution (100 mL) containing $Zn(NO_3)_2 \cdot 6H_2O$ (4.7 g) was added to another methanol solution (100 mL) containing 2-methylimidazole (15 g) under continuous stirring. The mixture was stirred for 24 hours at room temperature. The resulting white precipitate was collected by centrifugation, washed three times with methanol, and dried under vacuum at $80^\circ C$ to obtain ZIF-8₁₅₀. All subsequent steps remained identical to the Fe-N-C-70 synthesis. The final catalyst exhibited an average particle size of 150 nm.

Synthesis of Fe-N-C-400 Catalyst

A deionized water solution (48 mL) containing $Zn(OAc)_2 \cdot 2H_2O$ (0.65 g) was added to another deionized water solution (48 mL) containing 2-methylimidazole (7.3 g) under continuous stirring. After 5 min of mixing, the mixture solution was transferred to a PTFE liner for hydrothermal treatment at $120^\circ C$ for 6 h. The white precipitate was collected by centrifugation, washed three times with methanol, and dried under vacuum at $80^\circ C$ to obtain ZIF-8₄₀₀. Subsequent processing steps were identical to those described for Fe-N-C-70. The final catalyst had an average particle size of 400 nm.

Physical characterization

X-ray powder diffraction (XRD) patterns were collected using an XRD6000 diffractometer with $Cu K\alpha$ radiation ($\lambda = 0.154178$ nm). The diffraction data were recorded over a 2θ range of $5-90^\circ$ at a scan rate of $5^\circ min^{-1}$. Transmission electron microscopy (TEM) and energy dispersive spectroscopy (EDS) analyses were conducted on an FEI Tecnai G20 U-Twin microscope equipped with an EDX spectrometer operating at an acceleration voltage of 200 kV. Elemental composition was determined using inductively coupled plasma optical emission spectroscopy (ICP-OES) on a Agilent 5110. X-ray photoelectron spectroscopy (XPS) measurements were performed using an ESCALAB250Xi spectrometer with a monochromatic Al X-ray source (Al $K\alpha$, 1.4866 keV). Each spectrum was averaged from five scans, with the analysis chamber maintained at 10^{-7} Pa during data acquisition. The binding energy scale was calibrated by setting the C 1s peak to 284.8 eV to account for surface charging effects. Internal pores are intrinsic microscopic structures within the catalyst particles themselves, and their properties are determined by nitrogen adsorption-desorption tests. Specific surface areas were calculated using the Brunauer-Emmett-Teller (BET) method, while micropore surface areas were determined using the t-plot method. Pore size distributions were analyzed using the nonlocal density functional theory method. External surface area, defined as the non-micropore area, was calculated by subtracting the micropore surface area from the total BET surface area.

Stacked pores are microscopic pore structures that form within the catalyst layer due to the accumulation of catalyst particles and are typically tested using the mercury intrusion method (AutoPore IV 9500) at 25 °C, the catalysts were directly sprayed onto the membrane to form catalyst layer for stacking pore analysis to eliminate the impact of gas diffusion layer (GDL).

Electrochemical measurements

Electrochemical measurements were conducted using a standard three-electrode configuration on a Princeton VersaSTAT 3F electrochemical workstation equipped with a rotating disk electrode (RDE, 5 mm diameter, Pine Instruments). The RDE was polished to a mirror finish using 0.05 μm alumina suspension. All experiments were performed in 0.1 M KOH and 0.1 M HClO₄ electrolyte using a Hg/HgO reference electrode and a carbon rod counter electrode. The Hg/HgO reference electrode was calibrated via cyclic voltammetry (CV) using a purified Pt mesh working electrode in H₂-saturated 0.1 M KOH and 0.1 M HClO₄ electrolyte. Catalyst ink was prepared by ultrasonically dispersing the catalyst in ethanol containing 0.1 wt% Nafion. The ink was then deposited on glassy carbon electrodes and dried under infrared illumination to achieve a Fe-N-C loading of 0.6 mg cm⁻². For comparison, 20 wt% Pt/C was loaded at 25 μg_{Pt} cm⁻². All potentials reported herein are referenced to the reversible hydrogen electrode (RHE).

Oxygen reduction reaction (ORR) performance was evaluated following catalyst activation via CV in N₂-saturated 0.1 M KOH and 0.1 M HClO₄ from 0.0 to 1.2 V at a scan rate of 0.05 V s⁻¹. After achieving stable voltammograms, linear sweep voltammetry (LSV) measurements were performed in O₂-saturated 0.1 M KOH and 0.1 M HClO₄ from 0.0 to 1.2 V vs. RHE at a scan rate of 0.01 V s⁻¹ with electrode rotation at 1600 rpm. Fe-N-C catalyst stability was evaluated at 10000 cycles using cycles square wave testing in O₂-saturated 0.1 M KOH and 0.1 M HClO₄, cycling between 0.6 and 0.95 V vs. RHE with 3s holds at each potential.

Membrane electrode fabrication and Fuel cell Test

Membrane electrode assemblies (MEAs) were fabricated using the catalyst-coated membrane (CCM) method. The anode catalyst layer uses PtRu/C with a Pt loading of 0.2 mg cm⁻², while the cathode catalyst consists of Fe-N-C-70, Fe-N-C-150, and Fe-N-C-400 with a loading of 2.0 mg cm⁻². Piper Ion-A20-HCo3 is used as the anion exchange membrane (AEM), and Nafion-HP is used as the proton exchange membrane (PEM). The ionomer for AEMFC is PAP-TP-100, while Nafion is used for PEMFC. The catalyst ink was prepared by ultrasonically dispersing the catalyst powders with the commercial ionomer (PAP-TP-100) in isopropanol for 30 minutes. Prior to testing, the MEA for AEMFC was activated by immersion in 1 M KOH for 12 hours, while the MEA for PEMFC required hot pressing.

Fuel cell performance was evaluated using a Fuel Cell Testing System (850e, Scribner Associates Co.) under the following conditions: cell temperature at 80°C, reactant gas backpressure of 200 kPa (gauge) at both electrodes, and 100% relative humidity for all gas s

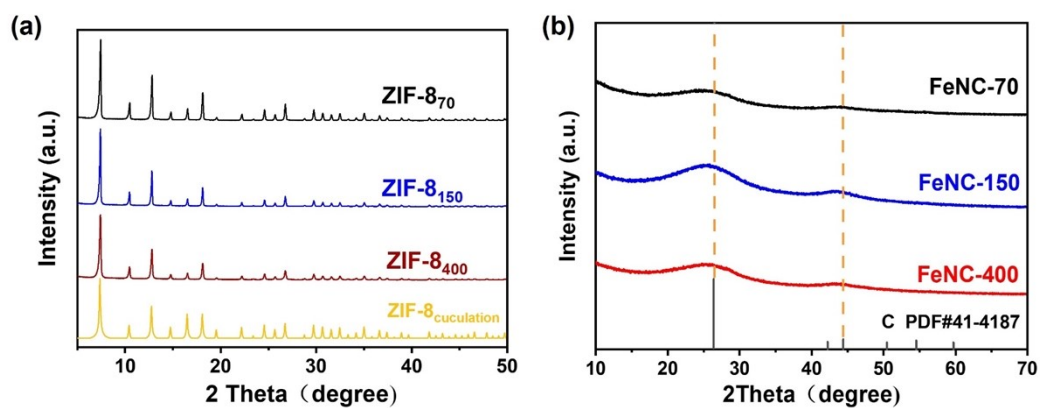


Fig S1. XRD patterns: ZIF-8 precursor (a), Fe-N-C-70, Fe-N-C-150 and Fe-N-C-400 catalysts (b).

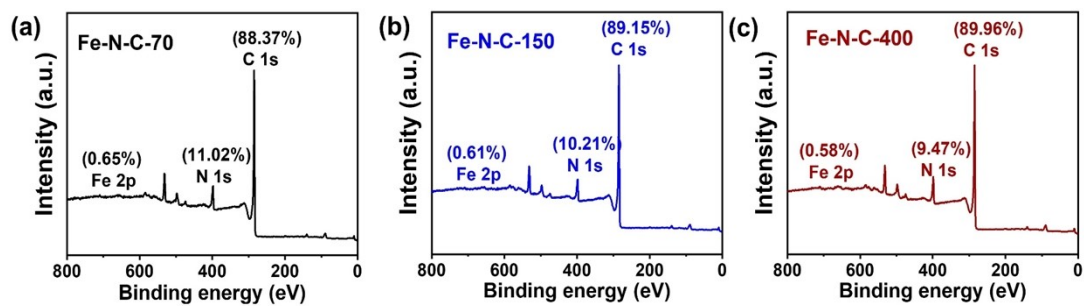


Fig S2. XPS gross spectra of the Fe-N-C-70, Fe-N-C-150 and Fe-N-C-400 catalysts.

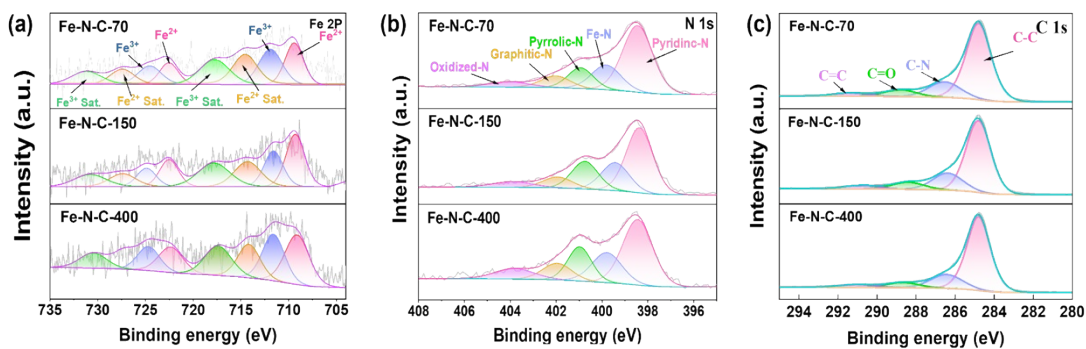


Fig S3. High-resolution Fe 2p (a), N1s (b) and C1s (C) XPS spectra of the Fe-N-C-70, Fe-N-C-150 and Fe-N-C-400 catalysts

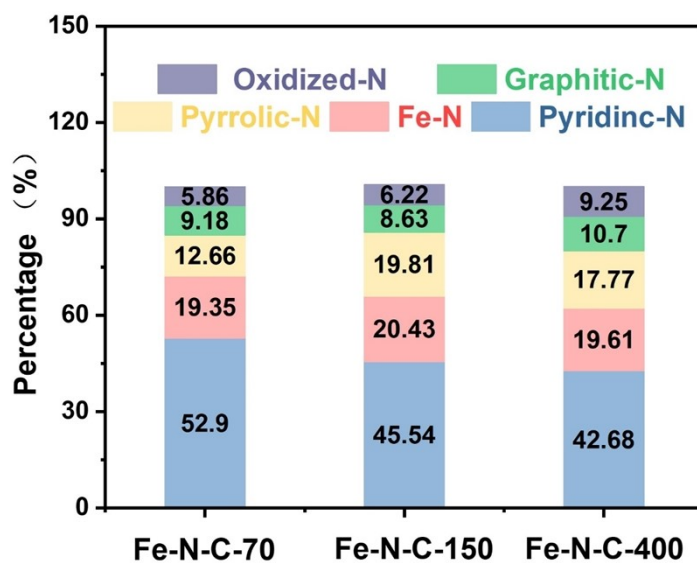


Fig S4. Compositional contents of NIs for Fe-N-C-70, Fe-N-C-150, and Fe-N-C-400 catalysts.

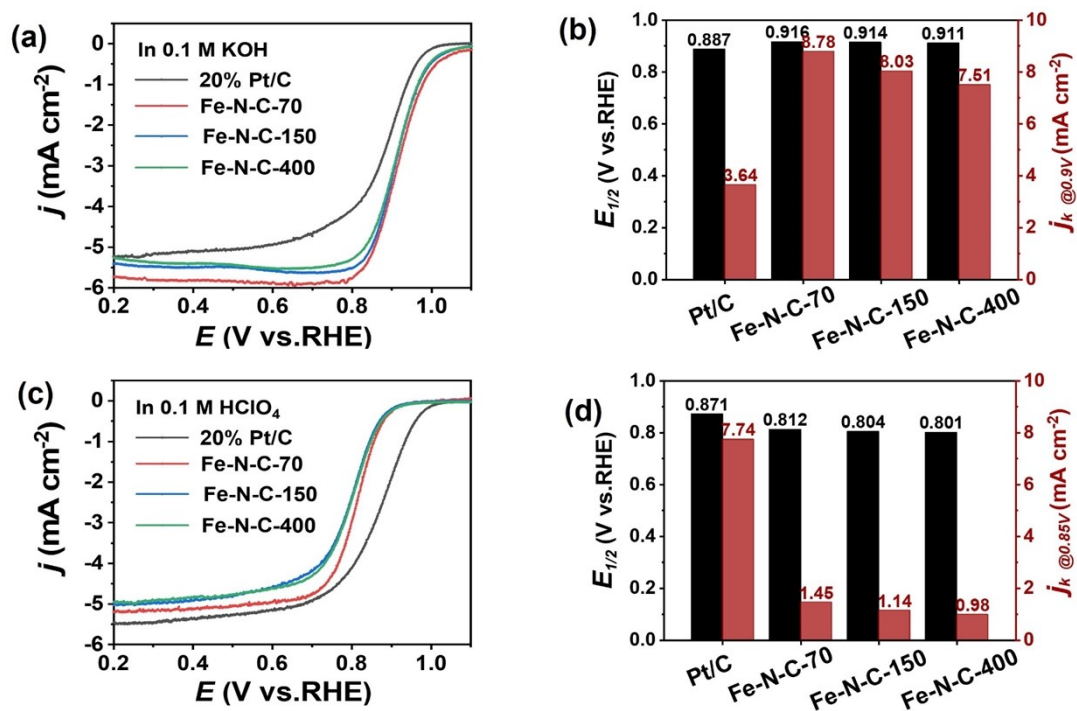


Fig S5. Fe-N-C-70, Fe-N-C-150, Fe-N-C-400 and Pt/C catalysts in 0.1 M KOH (a-b) and in 0.1M HClO₄ (c-d) RDE tests with a rotation speed of 1600 rpm and a catalyst loading of 0.6 mg cm⁻² for Fe-N-C and 25 μg_{Pt} cm⁻².

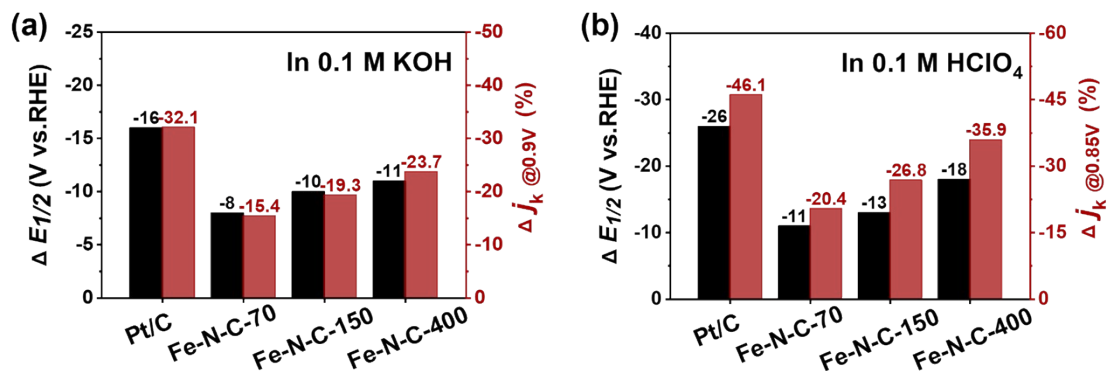


Fig S6. Performance attenuation statistics after 10000 cycles of square wave testing.

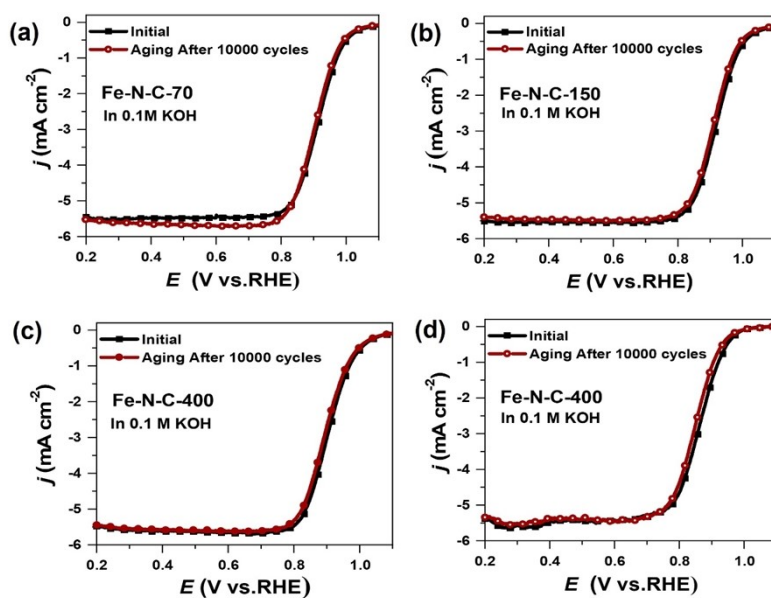


Fig S7. LSV curves before and after 10,000-cycle square wave stability tests of Fe-N-C-70, Fe-N-C-150, Fe-N-C-400, and 20%Pt/C catalysts in O₂-saturated 0.1M KOH (a-d).

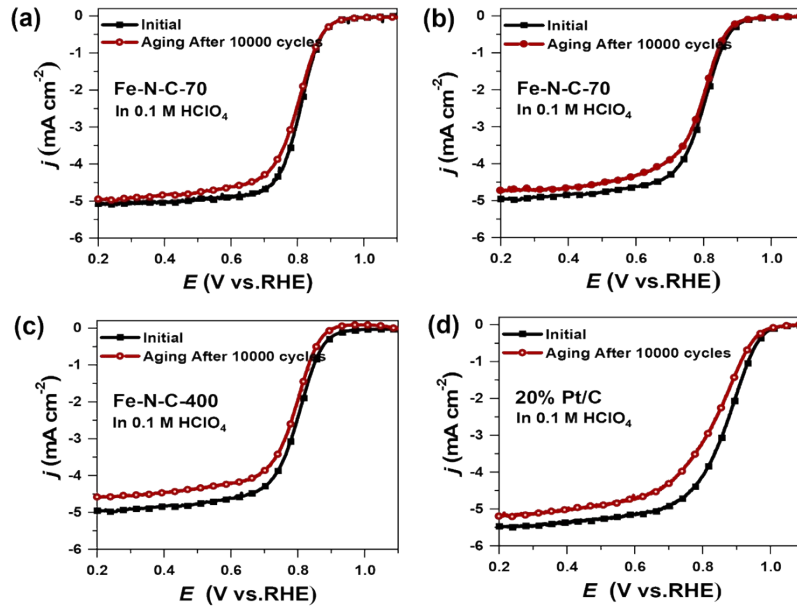


Fig S8. LSV curves before and after 10,000-cycle square wave stability tests of Fe-N-C-70, Fe-N-C-150, Fe-N-C-400, and 20%Pt/C catalysts in O_2 -saturated 0.1M $HClO_4$ (a-d).

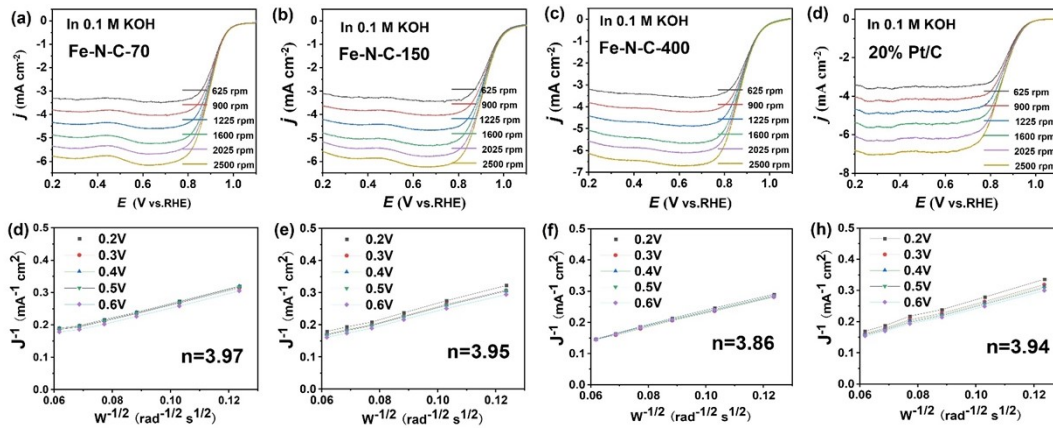


Fig S9. LSV curves at different rotating rates (a-d) and the corresponding K-L plots(e-f) of Fe-N-C-70, Fe-N-C-150, Fe-N-C-400 and Pt/C in 0.1 M KOH.

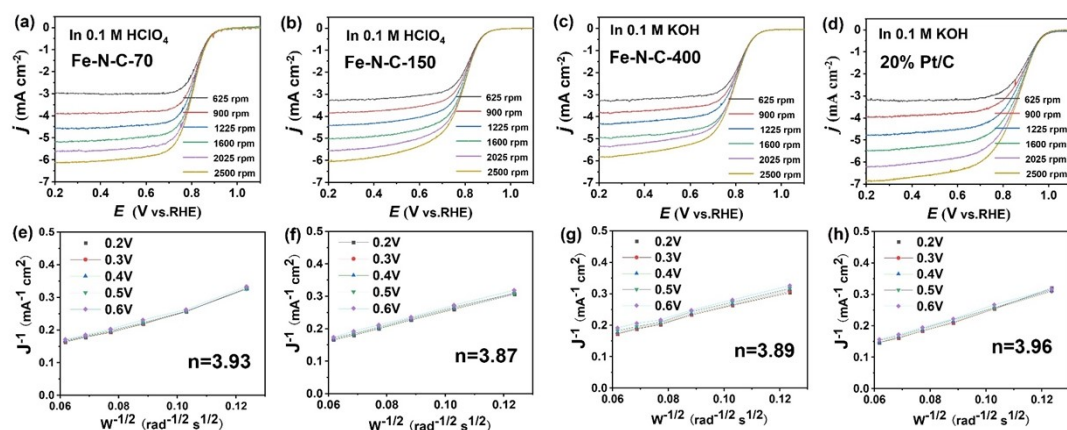


Fig S10. LSV curves at different rotating rates (a-d) and the corresponding K-L plots(e-f) of Fe-N-C-70, Fe-N-C-150, Fe-N-C-400 and Pt/C in 0.1 M HClO₄.

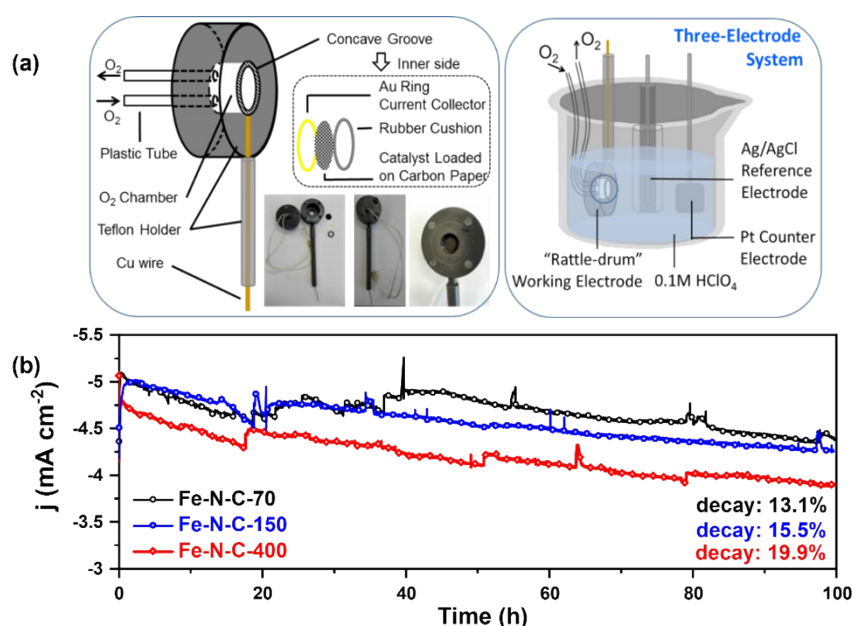


Fig S11. Schematic diagram of the 'rattle-drum' electrode working principle (a); The catalytic performance of Fe-N-C-70, Fe-N-C-150, and Fe-N-C-400 catalysts using the 'rattle-drum' electrode in O₂-saturated 0.1M KOH solution under constant potential testing, with a test potential of 0.7 V vs. RHE and a catalyst loading of 4 mg

Note S1: In alkaline medium, as shown in Fig. S6a-b, all Fe-N-C catalysts exhibited high half-wave potential ($E_{1/2}$) above 0.91 V and with kinetic current densities (j_k) of 8.78, 8.03 and 7.51 mA cm⁻² at 0.9 V for Fe-N-C-70, Fe-N-C-150 and Fe-N-C-400, respectively, which significantly outperformed the Pt/C. In acidic medium, as shown in Fig. S6c-d, the produced Fe-N-C catalyst showed a half-wave potential around 0.81, which lags behind that of Pt/C catalyst by only 60 mV. The kinetic current density ($j_k@0.85$), however, is approximately 18% of that Pt/C. After a 10,000-cycle potential pulse test, Fe-N-C-70 only exhibited an 8 mV negative shift with a 15.4% decay in kinetic current densities, while Fe-N-C-150 and Fe-N-C-400 showed slightly higher negative shifts of 10 and 11 mV, with corresponding kinetic current densities decays of 19.3% and 23.7%, respectively, whereas the degradation of the Pt/C catalyst was 16 mV and 32.1% in alkaline conditions (Fig. S7a and S8). In acidic medium, the resulting Fe-N-C catalyst shows a decay rate of less than 18 mV in the half-wave potential, which is slightly smaller than that of Pt/C under the same conditions. (Fig. S7band S9). Utilizing the Koutecky-Levich equation, the electron transfer number was quantified, and the Fe-N-C-x catalysts exhibited enhanced selectivity for four-electron ORR pathways in alkaline and acidic conditions (Fig.S10-11). These electrochemical analyses demonstrated that the Fe-N-C-x catalysts showed similar activity and excellent stability for ORR in the RDE test conditions.

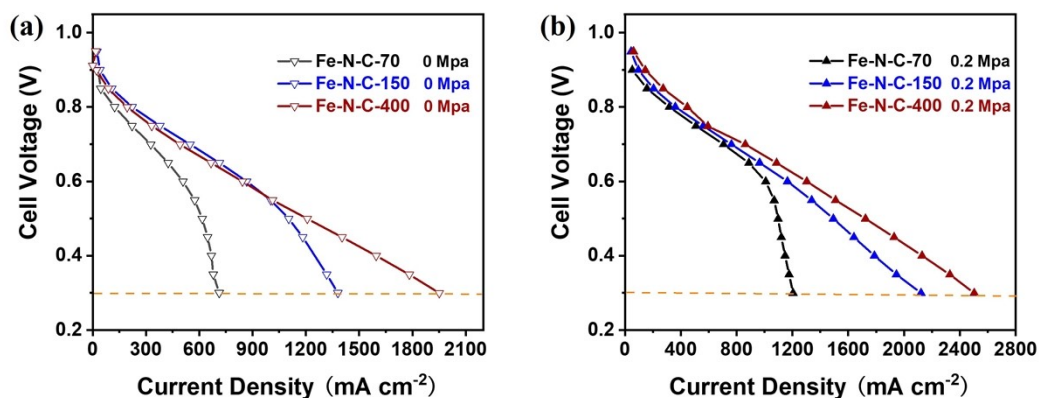


Fig S12. AEMFC I-V polarization curves at a back pressure of 0 MPa (a) and 0.2 MPa (b) of Fe-N-C-70, Fe-N-C-150 and Fe-N-C-400 catalyst.

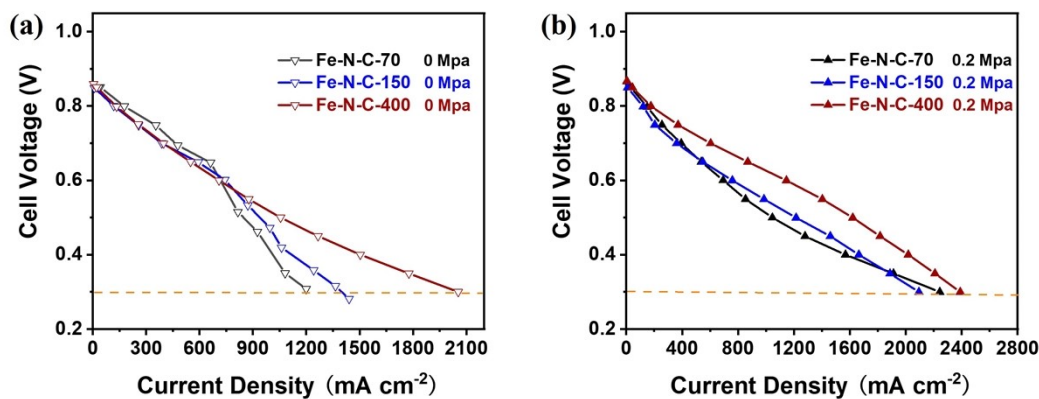


Fig S13. PEMFC I-V polarization curves at a back pressure of 0 MPa (a) and 0.2 MPa (b) of Fe-N-C-70, Fe-N-C-150 and Fe-N-C-400 catalyst.

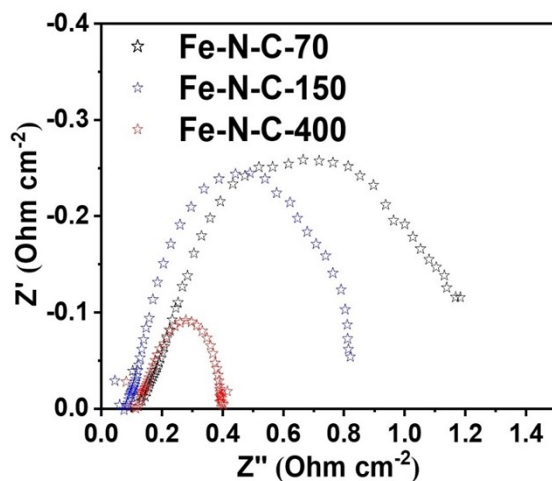


Fig S14. Electrochemical impedance spectroscopy of AEMFCs under 400 mA cm^{-2} and 0 MPa of back pressure.

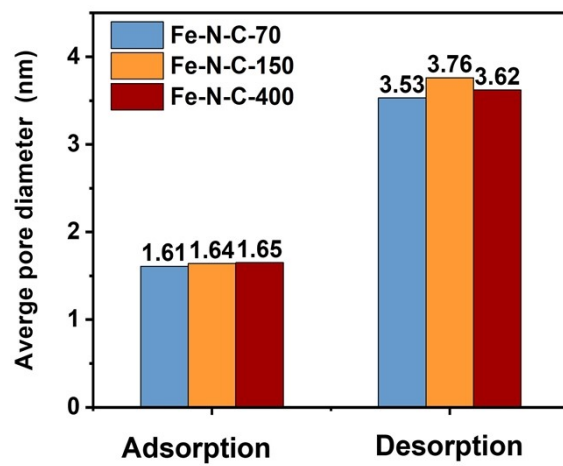


Fig S15. Average pore diameter for Barrett-Joyner-Halenda adsorption and desorption.

Supplementary Table S1. Weight ratio of Fe in Fe-N-C-70, Fe-N-C-150, and Fe-N-C-400 catalysts by ICP-OES

Catalyst	Fe (%)
Fe-N-C-70	2.17
Fe-N-C-150	2.13
Fe-N-C-400	1.94

Supplementary Table S2. Comparison of PEMFC performance of FeNC-x with other reported Fe-N-C catalysts.

Electrocatalyst	Catalyst Loading (mg cm ⁻²)		Peak power Density (W cm ⁻²)	Operating condition			Ref. No.
	Cathode	Anode (PGM)		Back Pressure (Mpa)	Tcell (°C)	Gas type (An/Ca)	
Fe-N-C-70	2	0.2	0.668	0.2 0.2	80	H2/O2	This work
Fe-N-C150	2	0.2	0.665	0.2	80	H2/O2	This work
Fe-N-C-400	2	0.2	0.816	0.2	80	H2/O2	This work
TPI@Z8(SiO2)- 650-C	2.7	0.2	1.18	0.25	80	H2/O2	1
Fe-N-C	3	0.1	735	0.2	80	H2/O2	2
FeNx-CNTs	4	0.3	1.16	0.2	60	H2/O2	3
1.5Fe-ZIF	2	0.2	670	0.1	80	H2/O2	4
sur-FeN4-HPC	2	0.2	0.79	0.2	80	H2/O2	5
FeNx/GP	2	0.2	0.74	0.2	80	H2/O2	6
ZIF-NC-0.5Fe-700	3.5	0.2	0.73	0.2	80	H2/O2	7

Supplementary Table S3. Comparison of AEMFC performance of FeNC-x with other reported Fe-N-C catalysts.

Electrocatalyst	Catalyst Loading (mg cm ⁻²)		Peak power Density (W cm ⁻²)	Operating condition			Ref. No.
	Cathode	Anode (PGM)		Back Pressure (Mpa)	Tcell (°C)	Gas type (An/Ca)	
Fe-N-C-70	2	0.2	0.607	0.2 0.2	80	H2/O2	This work
Fe-N-C150	2	0.2	0.745	0.2	80	H2/O2	This work
Fe-N-C-400	2	0.2	0.847	0.2	80	H2/O2	This work
Fe-N-C	3	0.1	0.51	0.2	80	H2/O2	2
Fe-N-C/CeO2	3	0.1	0.576	0.2	80	H2/O2	2
Fe-N-C/ZrO2	3	0.1	0.546	0.2	80	H2/O2	2
Comm Fe-N-C	1	0.6	2.05	0.20 0.15	80	H2/O2	8
FeNx-CNTs	4	0.3	1.15	0.2	60	H2/O2	3
Fe-CoPc/C	0.3	0.6	1.4	0.25	80	H2/O2	9
Fe/N/C Nanotubes	2	0.4	0.45	0.1	60	H2/O2	10
Fe-N-C	3.5	0.5	0.225	0.14	70	H2/O2	11
Fe-N/C	2.0	0.5	0.38	-	80	H2/O2	12

Supplementary Table S4. Comparison of PEMFC stability of FeNC-x with other reported Fe–N–C catalysts

Catalyst	Cell Conditions	Time (h)	Decay Rate	Decay	Ref. No.
Fe-N-C-70	0.8A cm ⁻²	20	0.97 mV h ⁻¹	3.27%	This work
Fe-N-C-150	0.8A cm ⁻²	20	1.36 mV h ⁻¹	4.94%	This work
Fe-N-C-400	0.8A cm ⁻²	20	2.65 mV h ⁻¹	7.90%	This work
TPI@Z8(SiO ₂)-650-C	0.5V	20	7.15 mA h ⁻¹	40%	1
Fe-N-C	0.7V	20	33.95 mA h ⁻¹	70%	2
Fe-N-C-ZrO ₂	0.7V	20	15.95 mA h ⁻¹	34%	2
Fe-N-C-CeO ₂	0.7V	20	17.5 mA h ⁻¹	40%	2
Fe-Zr/N/C	1 Acm ⁻²	20	8.34 mV h ⁻¹	25.3%	13
Fe-N-C	1 Acm ⁻²	20	22 mV h ⁻¹	72.3%	13
0.2Mela-Fe-NC	0.6V	21	21.65 mA h ⁻¹	87%	14
Fe/N/C(4mlm) OAc	0.5V	35	-	80.3%	15
SA-Fe/NG	0.5V	20	44 mA h ⁻¹	80%	16

Supplementary Table S5. Comparison of AEMFC stability of FeNC-x with other reported Fe-N-C catalysts

Catalyst	Cell Conditions	Time (h)	Decay Rate	Decay	Ref. No.
Fe-N-C-70	0.8 A cm ⁻²	15	5.51 mV h ⁻¹	31.9%	This work
Fe-N-C-150	0.8 A cm ⁻²	14.7	7.57 mV h ⁻¹	22.1%	This work
Fe-N-C-400	0.8 A cm ⁻²	14.7	10.7 mV h ⁻¹	14.2%	This work
Fe-N-C	0.7 V	1.5	-	63.9%	2
Fe-N-C-ZrO ₂	0.7V	20	-	34%	2
Fe-N-C-CeO ₂	0.7V	20	-	40%	2
AgNPs@Fe-N-C	0.25 mAcm ⁻²	10	10 mV h ⁻¹	11.4%	17
FeCo-N-C	0.6 A cm ⁻²	24	1.7 mV h ⁻¹	15%	18
Fe-N-C	0.6 A cm ⁻²	105	0.905 mV h ⁻¹	16%	19
Comm Fe-N-C	0.6 A cm ⁻²	150	0.46 mV h ⁻¹	16%	8

References

- 1 X. Wan, X. Liu, Y. Li, R. Yu, L. Zheng, W. Yan, H. Wang, M. Xu and J. Shui, *Nature Catalysis*, 2019, 2, 259-268.
- 2 Z. Xie, C. Zhang, Z. Xie, Z. Shen, L. Liu, L. Li, W. Ding and Z. Wei, *Science China Materials*, 2025, 68, 812-819.
- 3 Q. He, L. Zeng, J. Wang, J. Jiang, L. Zhang, J. Wang, W. Ding and Z. Wei, *Journal of Power Sources*, 2021, 489, 229499.
- 4 H. Zhang, H. T. Chung, D. A. Cullen, S. Wagner, U. I. Kramm, K. L. More, P. Zelenay and G. Wu, *Energy & Environmental Science*, 2019, 12, 2548-2558.
- 5 G. Chen, Y. An, S. Liu, F. Sun, H. Qi, H. Wu, Y. He, P. Liu, R. Shi and J. Zhang, *Energy & Environmental Science*, 2022, 15, 2619-2628.
- 6 X. Fu, N. Li, B. Ren, G. Jiang, Y. Liu, F. M. Hassan, D. Su, J. Zhu, L. Yang and Z. Bai, *Advanced Energy Materials*, 2019, 9, 1803737.
- 7 J. Li, H. Zhang, W. Samarakoon, W. Shan, D. A. Cullen, S. Karakalos, M. Chen, D. Gu, K. L. More and G. Wang, *Angewandte Chemie International Edition*, 2019, 58, 18971-18980.
- 8 H. Adabi, A. Shakouri, N. Ul Hassan, J. R. Varcoe, B. Zulevi, A. Serov, J. R. Regalbuto and W. E. Mustain, *Nature energy*, 2021, 6, 834-843.
- 9 L. Wang, M. Bellini, H. A. Miller and J. R. Varcoe, *Journal of Materials Chemistry A*, 2018, 6, 15404-15412.
- 10 H. Ren, Y. Wang, Y. Yang, X. Tang, Y. Peng, H. Peng, L. Xiao, J. Lu, H. D. Abruna and L. Zhuang, *Acs Catalysis*, 2017, 7, 6485-6492.
- 11 M. M. Hossen, K. Artyushkova, P. Atanassov and A. Serov, *Journal of Power Sources*, 2018, 375, 214-221.
- 12 Y. J. Sa, D.-J. Seo, J. Woo, J. T. Lim, J. Y. Cheon, S. Y. Yang, J. M. Lee, D. Kang, T. J. Shin and H. S. Shin, *Journal of the American Chemical Society*, 2016, 138, 15046-15056.
- 13 B. Chi, L. Zhang, X. Yang, Y. Zeng, Y. Deng, M. Liu, J. Huo, C. Li, X. Zhang and X. Shi, *ACS catalysis*, 2023, 13, 4221-4230.
- 14 Y. Li, S. Yin, L. Chen, X. Cheng, C. Wang, Y. Jiang and S. Sun, *Energy & Environmental Materials*, 2024, 7, e12611.
- 15 Y. Li, P. Zhang, L. Wan, Y. Zheng, X. Qu, H. Zhang, Y. Wang, K. Zaghbi, J. Yuan and S. Sun, *Advanced functional materials*, 2021, 31, 2009645.
- 16 L. Yang, D. Cheng, H. Xu, X. Zeng, X. Wan, J. Shui, Z. Xiang and D. Cao, *Proceedings of the National Academy of Sciences*, 2018, 115, 6626-6631.
- 17 Y. Yang, X. Xu, P. Sun, H. Xu, L. Yang, X. Zeng, Y. Huang, S. Wang and D. Cao, *Nano Energy*, 2022, 100, 107466.
- 18 K. Kisand, A. Sarapuu, J. C. Douglin, A. Kikas, A. Treshchalov, M. Käärrik, H.-M. Piirsoo, P. Paiste, J. Aruväli and J. Leis, *Acs Catalysis*, 2022, 12, 14050-14061.
- 19 H. Adabi, P. G. Santori, A. Shakouri, X. Peng, K. Yassin, I. G. Rasin, S. Brandon, D. R. Dekel, N. U. Hassan and M.-T. Sougrati, *Materials Today Advances*, 2021, 12, 100179.